Quantitative study of contrast enhancement in soft X-ray micrographs of insect eyes by tissue selective mass loss

Andreas Späth,[a] Benjamin Watts,[b] Lutz Thilo Wasserthal[c] and Rainer H. Fink[a,d]*

[a]Physical Chemistry 2 and ICMM, Friedrich Alexander Universität Erlangen-Nürnberg (FAU), Egerlandstrasse 3, Erlangen 91058, Germany, [b]Swiss Light Source, Paul Scherrer Institut, Villigen 5232, Switzerland, [c]Developmental Biology, Friedrich Alexander Universität Erlangen-Nürnberg, Staudtstrasse 5, Erlangen 91058, Germany, and [d]CENEM, Friedrich Alexander Universität Erlangen-Nürnberg, Egerlandstrasse 3, Erlangen 91058, Germany. *E-mail: rainer.fink@fau.de

Quantitative studies of soft X-ray induced radiation damage in zone-plate-based X-ray microspectroscopy have so far concentrated on investigations of homogeneous specimens. However, more complex materials can show unexpected radiation-induced behaviour. Here a quantitative radiochemical analysis of biological tissue from *Xantophan morganii praedicta* eyes is presented. Contrast enhancement due to tissue selective mass loss leading to a significant improvement of imaging quality is reported. Since conventional quantitative analysis of the absorbed dose cannot conclusively explain the experimental observations on photon-energy-dependent radiation damage, a significant contribution of photo- and secondary electrons to soft matter damage for photon energies above the investigated absorption edge is proposed.

Keywords: soft X-ray microspectroscopy; STXM; radiation damage; radiation chemistry.

1. Introduction

Zone-plate-based scanning transmission soft X-ray microspectroscopy (STXM) is a well established method for the morphological and chemical characterization of various biomaterials with nano-scale resolution in the so-called water window (Kirz *et al.*, 1995; Leung *et al.*, 2010). Recently investigated systems range from protein-coated biocompatible polymer films (Hitchcock *et al.*, 2005) and biofibres (Rousseau *et al.*, 2007; Fink *et al.*, 2009) to pathological studies of blood cells (Wang *et al.*, 2012) and metabolism tracking in bacteria (Toner *et al.*, 2005; Christl *et al.*, 2012). In STXM the image contrast can be enhanced by tuning the photon energy to take advantage of resonant imaging (Ade & Hitchcock, 2008). The resolution limit depends on the outermost zone width of the applied Fresnel zone plate and can reach to approximately 10 nm (Vila-Comamala *et al.*, 2009).

Owing to the high sensitivity of biomaterials to ionizing radiation, the study and control of radiation damage plays a large role in X-ray microscopy of biological specimens (Kirz *et al.*, 1995; Henderson, 1995; Teng & Moffat, 2000; Howells *et al.*, 2009). Extensive microspectroscopic studies have revealed that X-ray-induced radiation damage mainly results in the cleavage of chemical bonds and the evaporation of small volatile molecules like CO_2, NH_3, H_2O or radical species resulting in a significant loss of mass (Choi *et al.*, 1988; Beetz &

Jacobsen, 2003; Wang *et al.*, 2009*a*). The loss of carbonyl functionalities and bond cleavage at ester and amide groups has been found to be especially prevalent within several polymers as well as biomacromolecules (Coffey *et al.*, 2002; Wang *et al.*, 2009*b*; Späth *et al.*, 2014). After bond scission, relaxation of the electronic states can lead to the formation of new $C=C$ bonds (Zhang *et al.*, 1995; Coffey *et al.*, 2002; Tzvetkov *et al.*, 2014). The majority of radiation-induced bond cleavages are actually caused by secondary electrons and to some extent by the initial photoabsorption process (Cazaux, 1997; Wang *et al.*, 2009*a*). While the primary absorption event can only affect the direct neighbourhood, secondary electrons have dozens of interactions during their propagation through the material and induce further electron release cascades (Nikjoo *et al.*, 1997; Ziaja *et al.*, 2001).

Quantitative studies of radiation damage usually consider the energy uptake within the irradiated specimen volume during exposure by calculation of the absorbed doses (Sayre *et al.*, 1977; Wang *et al.*, 2009*b*; Leontowich *et al.*, 2012). The comparison of these absorbed doses with the microscopically detected mass loss or the spectroscopically detected decay of certain absorption resonances can be used to determine a critical dose that is helpful in preventing a spoiling of the recorded data by sample decomposition (Rightor *et al.*, 1997; Wang *et al.*, 2009*a*). However, critical doses vary with the applied photon energy. This finding gives a hint that the

concept of absorbed dose does not fully describe the photon-energy-dependent radiation-induced chemical processes during X-ray microspectroscopic investigations.

A common and well established approach to minimizing radiation-induced processes in X-ray microspectroscopy is the application of cryogenic techniques (Schneider, 1998; Maser *et al.*, 2000; Larabell & Nugent, 2010). It has been demonstrated that cryo-microscopy can significantly reduce mass loss and morphological degradation by fixation of the radiation chemistry products, but chemical decomposition is not prevented (Beetz & Jacobsen, 2003). A significant reduction of X-ray-induced decomposition requires temperatures of 50 K and below, especially for radiation-sensitive biomaterials (Meents *et al.*, 2010). Recent developments in polymer science show that radiation damage is not necessarily a disadvantageous effect, but can also be employed for novel applications, *e.g.* chemically selective and maskless nanolithography (Wang *et al.*, 2007; Leontowich & Hitchcock, 2011).

Within this paper we present the X-ray-induced decomposition effects on the functional structure of eye tissue from the hawk moth *Xantophan morganii praedicta* (Morgan's Sphinx). *X. morganii praedicta* played a role in the discussions about Charles Darwin's theory of evolution, since Darwin was able to predict the existence of this moth in Madagascar from his studies on the fertilization of endemic orchids years before the insect was actually discovered (Darwin, 1862). During soft X-ray microscopy investigations of the moth eye anatomy, we discovered a significant contrast enhancement at previously irradiated sample positions due to selective mass loss from functionally different tissue. To explore the effects in more detail, we include a dose- and energy-dependent evaluation of this effect and discuss the chemical degradation processes. The quantitative evaluation of the absorbed dose, however, does not provide a direct correlation with beam-damage-induced mass loss when different excitation energies are employed. Thus, the contribution of radiation-chemistry-based photon-energy-dependent decomposition enhancement and photo-electron generation has to be considered.

2. Experimental

The hawk moths for this investigation originated from long-term laboratory breeding. Eye specimens of deceased moths were microtomed and fixed on standard copper grids for transmission electron microscopy (TEM) and STXM imaging. Samples investigated by TEM were fixed with OsO_4 and stained with toluidine blue in advance. STXM samples were sliced to 100 nm thickness (according to interference colour), vacuum dried and measured in He atmosphere ($\sim$300 mbar after pumping to 10^{-4} mbar) to prevent effects of residual water on the radiation chemistry. STXM experiments were performed at beamline 5.3.2.2 at the Advanced Light Source (ALS), Berkeley, USA (Warwick *et al.*, 2002; Kilcoyne *et al.*, 2003). The standard STXM set-up uses high-brilliance synchrotron radiation light that is focused on the sample by a Fresnel zone plate. The sample is raster-scanned with inter-ferometric control through the focal spot. The transmitted

photon intensity is recorded by a photomultiplier tube (PMT) with a phosphor powder scintillator to convert X-rays into visible light. A nitrogen gas filter was used for higher-order suppression and the monochromator slits were set to 60 µm (entrance slit) and 30 µm (horizontal and vertical exit slit). Near-edge X-ray absorption fine-structure (NEXAFS) spectra were recorded by consecutive scanning of the investigated area with varying photon energy. The spectra were normalized and evaluated with the program package *aXis2000*.

3. Results and discussion

Fig. 1 shows a TEM micrograph of a typical hawk moth eye tissue stained with toluidine blue to visualize the morphology of this specimen. The micrograph provides detailed insight into the anatomy of the investigated tissue. The structure of the compound eye units (ommatidia) (Briscoe, 2008) is clearly resolved with good signal-to-noise ratio. While pigment cells and the compact rhabdom show a relatively low transmittance, eye cell bodies and tracheae, *i.e.* tubular structures serving as respiratory system of the tissue, show up as bright regions due to their lower material density. Although TEM is a well established technique for the microscopy of biological samples (Engel, 1991; Kourkoutis *et al.*, 2012), the major advantage of STXM is the possibility of resonant imaging, which obviates the use of contrast agents and reduces the deposited energy dose (Ade & Hitchcock, 2008).

However, from the STXM micrograph of *X. morganii praedicta* eye tissue at 288.7 eV depicted in Fig. 2 it can be seen that the initial contrast of rhabdom and tracheae/cell bodies at the C 1*s* edge is rather low. Remarkably, the re-imaging of previously recorded sample areas resulted in a significantly better contrast. Therefore, we pre-irradiated, for 3.5 ms, a series of 10 µm × 2 µm sample areas with various photon energies: 285.1 eV (C *K*-edge $\pi^*_{C=C-C}$), 288.7 eV ($\pi^*_{O=C-OR}$), 320 eV (off resonance), 390.0 eV (off resonance), 400.7 eV (N *K*-edge π^*_{CONH2}) and 532.0 eV (O *K*-edge $\pi^*_{O=C-OR}$) (Zubavichus *et al.*, 2005). The lowest two photon energies were selected to correspond to the most significant spectral features in the NEXAFS spectrum of this specimen (see Fig. 3). The
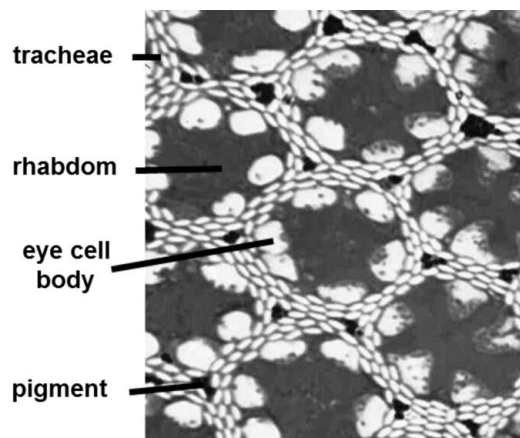
Figure 1
TEM micrograph of hawk moth eye tissue with OsO_4 fixation and toluidine blue staining.
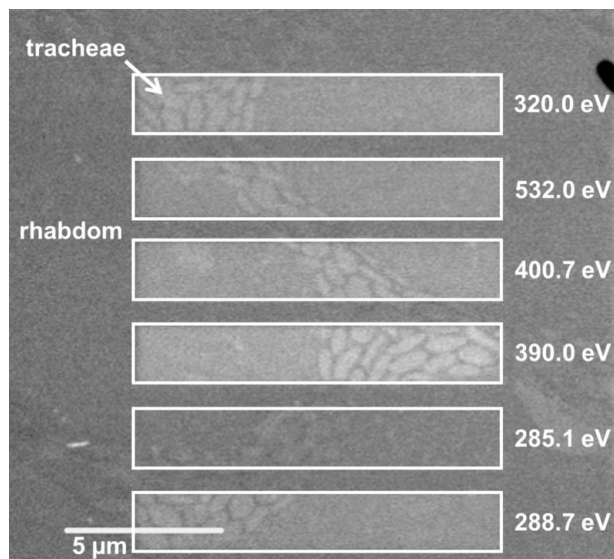
Figure 2
STXM micrograph of *X. morganii praedicta* eye tissue at 288.7 eV. The white-framed areas were previously irradiated with the respective photon energy denoted on the right side of the frames for 3.5 ms.

pixel size during irradiation was chosen close to the diameter of the focal spot (~20 nm) to achieve a homogeneous dose distribution. Fig. 2 shows a micrograph including all these pre-irradiated areas and was recorded with a low dwell time of 1 ms in order to minimize further sample damage.

It is clearly visible that the contrast between the rhabdom and tracheae is significantly enhanced for all pre-irradiation energies except for 285.1 eV. The strongest effect appears for 390.0 eV, followed by 400.7 eV, while 288.7, 320.0 and 532.0 eV give a comparable enhancement in contrast.
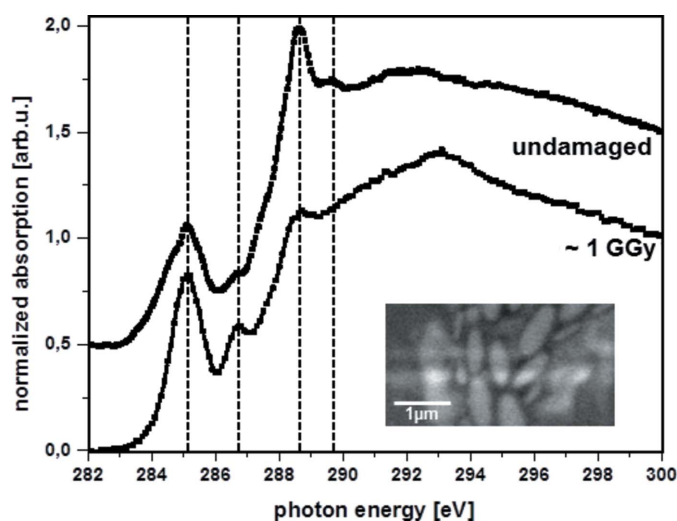
Figure 3
Normalized NEXAFS spectra of *X. morganii praedicta* tissue without previous X-ray exposure and after deposition of an X-ray dose of about 1 GGy at 288.7 eV photon energy. The spectrum of undamaged material is shifted by 0.5 in the *y*-axis for better representation. The inset in the lower right corner shows an off-resonance micrograph (transmitted intensity) of the sample demonstrating radiation mass loss due to previous line scans (brighter stripes).

For a quantitative analysis of these findings, we calculated the absorbed dose d using the formula (Leontowich *et al.*, 2012)

$$d = FEt/KV\rho, \tag{1}$$

where F is the photon absorption rate per second that is calculated from the number of incident photons I_0 (photon flux) and the energy-dependent optical density OD by

$$F = I_0[1 - \exp(-\text{OD})], \tag{2}$$

E is the respective photon energy, t is the irradiation time and V is the irradiated sample volume. K is the photon-energy-dependent detector efficiency that was taken from previous characterizations of the same detector set-up from the literature (Kilcoyne *et al.*, 2003).

Contrary to many quantitative studies of beam damage in the literature that concentrate on one specific material (Beetz & Jacobsen, 2003; Wang *et al.*, 2009a; Leontowich *et al.*, 2012), the investigated eye tissue is chemically and morphologically very complex. Therefore, it is not feasible to give an absolute value for the material density ρ; it would be necessary to determine the local density at every pixel. On the other hand, a high accuracy of the absolute values of the dose is less important than the relative values for the present evaluation. Therefore, we estimated a (mass) density of 250 kg m^{-3} (corresponding to heavy foam materials) for the more compact rhabdom. Since the spectra of the structures are not significantly different and the thickness of the microtomed slices is homogeneous, the optical density at a given photon energy simply depends on the density of the material. Calculation of average pixel values resulted in an optical density ratio of 1.4 for the two structures, giving an estimated density of 180 kg m^{-3} for the tracheae structures. Owing to the relatively short exposure times, a mass-loss-induced reduction of OD during the irradiation can be neglected for the dose calculation.

The resulting energy and flux-dependent X-ray doses for the pre-irradiation series are summarized in Table 1. The contrast rhabdom *versus* tracheae, C, for the micrograph in Fig. 2 was calculated using the average transmitted intensities I of both structures by

$$C = I_{\text{rhabdom}}/I_{\text{tracheae}}. \tag{3}$$

The contrast enhancement factor is defined by the division of the respective value of C by 0.25, which corresponds to the C-value without previous irradiation.

The calculated doses of 8–16 MGy are in the typical range where bond scission can no longer be neglected in X-ray absorption experiments (Henderson, 1990; Beetz & Jacobsen, 2003). We found no significant differences in the C K-edge NEXAFS spectra of rhabdom and tracheae tissue (discussed below) and therefore it is not surprising that the absorbed doses are more or less identical for both structures. Considering the reduced photon flux in the low-energy regime, the resonant energies cause an increased energy uptake. On the contrary, the calculated doses at 390 eV are lowest, despite coinciding with the highest observed photon flux. Comparing

Table 1
Absorbed doses during pre-irradiation with various photon energies and resulting contrast enhancement.

Energy (eV)	Photon flux (10³ photons s⁻¹)	Optical density (a.u.)†		Absorbed dose (MGy)		Contrast tracheae *versus* rhabdom (%)	Contrast enhancement
		Tracheae	Rhabdom	Tracheae	Rhabdom		
No irradiation	0	N/A	N/A	0	0	0.25	N/A
285.1	4.7	0.031	0.045	23	24	0.25	1.0
288.7	4.0	0.046	0.048	28	22	0.97	3.9
320.0	7.9	0.016	0.020	16	14	1.20	4.8
390.0	10.5	0.007	0.010	7	7	4.03	16.0
400.7	9.6	0.012	0.018	10	11	2.88	11.5
532.0	9.5	0.009	0.016	8	10	1.50	4.8

† OD not normalized.

the different values in Table 1, the observed mass loss and resulting contrast enhancement do not directly correlate with the absorbed dose. Furthermore, the lack of mass loss at the resonance energy 285.1 eV is remarkable and motivates efforts to gain a more detailed understanding of the beam-induced radiochemical processes during X-ray exposure of this specimen.

Fig. 3 presents two C K-edge NEXAFS spectra of *X. morganii praedicta* eye tissue recorded without and with previous X-ray dose of about 1 GGy (300 ms exposure at 288.7 eV photon energy). The X-ray exposure leads to a strong decay in the resonance features at 288.7 and 289.7 eV that are usually assigned to π^* transitions from ester groups. Also the shoulder at about 288.3 eV that arises from amide groups (π^*_{CONH2}) shows a decrease after irradiation. At the same time the peaks at 285.1 ($\pi^*_{C=C-C}$) and 286.8 eV ($\pi^*_{C=O}$) are significantly increased. In addition, a new broad spectral feature around 293 eV arises that is assigned to σ^*_{C-C} transitions. From this behaviour we conclude a beam-induced cleavage of ester and amide groups within the investigated tissue as major process responsible for the observed radiation damage. After the initial bond cleavage, new carbon–carbon bonds can be formed and also the amount of aldehyde end groups and carbonyl groups increases. Since the spectra are normalized for optimum representation of radiation chemical aspects, mass loss is not directly visible. Therefore, we added an inset showing a STXM micrograph of a sample area previously irradiated with linescans. These scans are visible as brighter stripes. Owing to off-resonance imaging conditions (530 eV) this behaviour directly indicates the mass loss. The mass loss arises from the removal of small volatile molecules like CO_2 or NH_3, similar to investigations of the biomacro-molecule fibrinogen (Wang *et al.*, 2009b).

Bond cleavage in soft X-ray microscopy is mainly considered to be induced by electrons from Auger decays that follow the primary photoabsorption and excitation of core electrons (Cazaux, 1997). The Auger cascades generate holes in or close to the valence band of the material weakening neighbouring bonds, and the released Auger electrons are able to induce bond scission by scattering. Auger emissions in C, N and O are dominated by KLL-transitions, yielding electrons with kinetic energies of 272 eV, 379 eV or 503 eV, respectively (Mrocz-kowski & Lichtman, 1985). Also, the inelastic mean free path of these primary Auger electrons within carbonaceous

material is just around 1 nm and their thermalization induces dozens of secondary electrons (Ziaja *et al.*, 2001; Tanuma *et al.*, 2011). Therefore, the secondary-electron-induced decomposition propagates over a large number of neighbouring molecules. The secondary electron cascade should in any case reach several of the preferentially cleaved ester and amide groups. The high mass loss at the corresponding resonance energies of these groups, *i.e.* 288.7 eV, 400.7 eV and 532.0 eV, strongly indicates a strong contribution of the primary photoabsorption process. The excitation of core electrons into antibonding orbitals weakens the respective bonds and enhances the probability of their cleavage. This consideration also explains the insignificant mass loss at 285.1 eV. This resonance is assigned to carbon–carbon bonds that seem to be more stable and the photon energy is also lower than the resonance of the ester and amide groups. Therefore mass loss due to the primary photoabsorption process is almost negligible at this energy.

Considering the off-resonant energies, however, we expect the main contribution to be from secondary electron generation and therefore a strong correlation to the number of absorbed photons. Although the X-ray absorption cross section at the C K-edge is still relatively high at 320 eV, it is strongly decreased at 390 eV (Henke *et al.*, 1993). With respect to the resulting small absorbed dose, the discussion of the radiation chemical processes within the investigated tissue does not explain why illumination at 390 eV provides the highest mass loss, while absorption and dose are comparably low.

An important issue in the quantitative analysis of absorbed dose not discussed so far is the detector efficiency. For our dose calculations we used values previously reported by Kilcoyne *et al.* (2003) for the same detector set-up. The energy dependence of these values is dominated by the luminescence of the phosphor scintillators in front of the PMT detector which is continuously increasing over the investigated energy regime (Fakra *et al.*, 2004). A constant degradation of the phosphor powder leads to significant reduction of the detector efficiency over time, but should not affect the qualitative energy dependence. Another contribution to the detector efficiency is the signal attenuation due to material deposits on the detector. Especially during experiments with high mass loss we might expect a higher pollution of the detector. The latter aspect makes an entire quantitative treatment of the

energy-dependent detector efficiency extremely complicated and further studies must also consider the development of a time-dependent control of the detected signal. On the other hand, deposits will attenuate the detector signal mainly in the energy regime of the resonances (especially carbon). Therefore the main contributions to the detector efficiency hint at an underestimation of the signal at 390 eV compared with the carbon resonance regime. In summary, a detailed consideration of the detector efficiency would result in higher dose estimates at the resonance energies and even lower dose estimates at 390 eV and so cannot account for our observations.

We therefore conclude that the generation of photoelectrons makes a strong contribution to the observed radiation damage at 390 eV. For photon energies well above the resonance energy, a photoexcited electron is not lifted into an unoccupied state, but is released as a photoelectron (*cf.* Fig. 4). The origin of the resulting core hole has no influence on the subsequent Auger cascade. The major difference is, however, the number of electrons released per absorbed photon. In the case of photoelectron release, an additional primary electron contributes to radiation chemical processes. Furthermore, the energy distribution of the Auger electrons is determined by the energy levels of the electrons involved in the cascade and will not change with illumination energy. The kinetic energy of the photoelectrons and therefore their potential to induce bond cleavage depends on the photon energy.

Studies on the decomposition effects of low-energy electrons on DNA showed that the kinetic energy of the electrons and their damage potential show a strong correlated increase above 15 eV due to the increasing energy deposition (Nikjoo *et al.*, 1997; Boudaïffa *et al.*, 2000). Although the photoionization cross section of the C 1*s* electron is decreasing from 320 eV to 390 eV by about 35% (Yeh, 1993), the increasing damage potential and range of the photoelectrons more than compensates for this decline. Therefore, we detect an increasing contribution from photoelectron-induced damage when the photon energy is changed from 320 to 390 eV. At the N *K*-edge (400.7 eV) resonant absorption becomes dominant again (Cazaux, 1997).
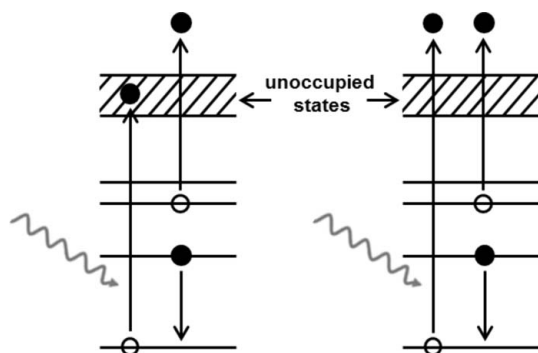
Figure 4
Origin of Auger cascades due to X-ray absorption: resonant excitation into an unoccupied state (left) leads to the generation of one free Auger electron (single-charged final state). Higher photon energies lead to the generation of a photoelectron (right) and the subsequent Auger process releases a second electron (double-charged final state).

The complete radiochemical analysis of the investigated contrast enhancement in microtomed slices of *X. morganii praedicta* eyes shows that a proper discussion of X-ray-induced decomposition and mass loss at various photon energies must go beyond the concept of absorbed dose. The number of radiation damage events (that is a direct measure for the amount of cleaved bonds and microscopically visible mass loss) is proportional to the absorbed energy dose only as long as the photon energy remains constant. For varying photon energies, the material-dependent probability of bond cleavage has to be considered. Therefore we have to respect three decomposition pathways with different energy dependencies:

(i) Direct bond cleavage due to the primary absorption process and excitation of core electrons into antibonding orbitals. The probability of this process is proportional to the absorption cross section of the preferentially cleaved functional groups. Therefore the contribution of this pathway is high for resonant excitation and low for other photon energies.

(ii) Bond scission by interaction with Auger electrons or secondary electrons originating from Auger-cascades (mainly due to inelastic scattering). The Auger yield at the *K*-edges of C, N and O is above 99% (Krause, 1979). Since the energies of the primary Auger electrons are given by the energy levels of the investigated material and independent of the photon energy, this pathway is proportional to the absorption spectrum of the specimen and closely corresponds to the concept of absorbed dose for most soft matter samples.

(iii) Bond scission by interaction with photoelectrons or secondary electrons originating from photoelectron release. Photoionization cross sections have been calculated and tabulated for all relevant elements and their subshells (Yeh, 1993). The damage potential of low-energy electrons is rather complex below a kinetic energy of 15 eV and increases continuously for higher energies (Nikjoo *et al.*, 1997; Boudaïffa *et al.*, 2000). Therefore, this pathway plays an increasing role for photon energies above the investigated absorption edge.

It should be mentioned that the contribution of pathways (ii) and (iii) are reduced in the surface region of the specimen due to the adjacent vacuum being a net electron sink (Cazaux, 1997). Referring to our investigations of the *X. morganii praedicta* eye tissue, we are dealing with tissues of different porosity, *i.e.* the density of tracheae is lower than for the rhabdom. The higher porosity only creates a larger internal surface. Since the electrons do not escape with different probability from either material, the impact of secondary electrons is not affected by porosity.

After a detailed quantitative study of the radiochemical processes we can exclude the appearance of different decomposition mechanisms within the rhabdom and tracheae parts of the investigated eye specimen. Therefore we propose that the contrast enhancement effect mainly originates from the structural differences of the tissues. The release of volatile decomposition products to the vacuum will rather happen at surface molecules than from the bulk. Owing to the porosity of the material, low-density tissues, in our case tracheae and eye

research papers
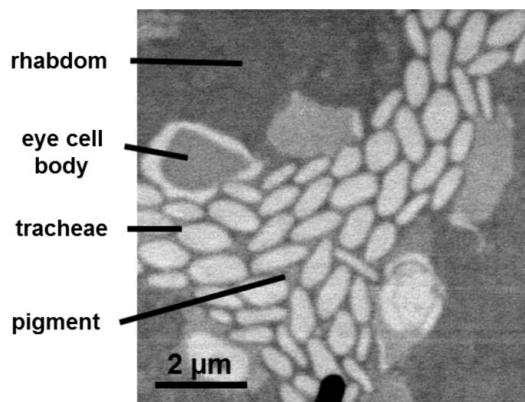
Figure 5
STXM micrograph of *X. morganii praedicta* tissue at 400.7 eV after previous exposure to an X-ray dose of about 15 MGy above the $\pi^*_{O=C-OR}$ resonance.

cell bodies, will provide a higher release per mass unit than materials with higher density (rhabdom). This effect over-compensates the potentially higher release of secondary electrons to the vacuum from the tracheae structures that was discussed above. The density deviation within the investigated tissues is high enough that already moderate doses lead to a significant enhancement of the X-ray absorption contrast.

The STXM micrograph of the *X. morganii praedicta* eye tissue depicted in Fig. 5 was recorded at a photon energy of 400.7 eV after previous irradiation with a dose of about 15 MGy above the $\pi^*_{O=C-OR}$ resonance to employ the experience gained from the dosimetric and radiochemical analysis. This results in an excellent morphological contrast that is comparable with the TEM micrograph of the stained tissue in Fig. 1. This demonstrates how STXM allowed us to identify that the eye cell bodies are not homogeneous in terms of structural density, which is difficult to detect with TEM. We should emphasize again that STXM does not require contrast agents due to the tunable photon energy.

4. Conclusions and outlook

In conclusion, we have presented a detailed dosimetric and radiochemical analysis of radiation damage during STXM imaging of *X. morganii praedicta* eye tissue. We discussed the observed mass loss by means of NEXAFS spectroscopy and compared it quantitatively with estimated absorbed energy doses. Mass loss is strongly dependent on the applied photon energy. Since it is mainly caused by the cleavage of ester and amide groups, we observe enhanced mass loss at resonance energies of these functionalities. The discrepancy of mass loss and absorbed dose at the non-resonant energy 390 eV is explained by a significant contribution of photoelectrons to the radiation damage that are released in addition to Auger electrons at energies high above the C 1*s* resonance.

These considerations lead to the postulation of a modified description for the quantitative analysis of X-ray radiation damage. The common approach based on the calculation of absorbed doses gives a proper treatment of radiation damage

only as long as the photon energy stays constant. When the photon energy is varied, the number of radiochemical decomposition events is not directly proportional to the number of absorbed photons. Various damage mechanisms contributing to radiation chemistry, namely photoexcitation into antibonding orbitals, Auger cascades and photoelectron generation, have energy-dependent intensities and damage probabilities. Future studies will concentrate on a more detailed investigation of energy-dependent radiation damage. Therefore it is more suitable to evaluate mass loss on homogeneous and well described model systems, *e.g.* PMMA or a fluoropolymer. Such studies will allow for a quantitative analysis of the various decomposition pathways with respect to their particular interaction cross sections and the energy-dependent damage potential of the released secondary electrons. These evaluations could contribute to the postulation of an advanced formalism for a quantitative treatment of X-ray-induced radiation damage that enhances the common model of absorbed doses.

The X-ray-induced mass loss occurring during our investigations of the *X. morganii praedicta* specimen leads to a significant contrast enhancement compared with unexposed sample regions. This contrast enhancement is caused by a less restricted release of volatile decomposition products from structures with lower density. This observation is of high interest for future microspectroscopic investigations of similar biological (and inorganic) specimens with low initial spectroscopic contrast, but high porosity (especially in the dry state). Previous irradiation with moderate doses at the right energy can improve the quality of soft X-ray imaging of suitable material mixtures significantly. Employing this effect extends the potential of soft X-ray absorption microscopy for the investigation of complex nanostructures and has the potential to foster further soft X-ray microscopy of biosamples. Of course, the suitability of the specimen, as well as its radiochemistry, have to be considered to exclude severe structural damage by pre-irradiation.

Further investigations will also concentrate on the adaption of our radiation damage model and the concept of contrast enhancement to TEM. Since secondary electrons play a major role in X-ray radiation damage, we propose similar decomposition paths for various soft matter specimens during electron microscopy.

References

Ade, H. & Hitchcock, A. P. (2008). *Polymer*, **49**, 643–675.
Beetz, T. & Jacobsen, C. (2003). *J. Synchrotron Rad.* **10**, 280–283.
Boudaïffa, B., Cloutier, P., Hunting, D., Huels, M. A. & Sanche, L. (2000). *Science*, **287**, 1658–1660.

Briscoe, A. D. (2008). *J. Exp. Biol.* **211**, 1805–1813.

Cazaux, J. (1997). *J. Microsc.* **188**, 106–124.

Choi, J. O., Moore, J. A., Corelli, J. C., Silverman, J. P. & Bakhru, H. (1988). *J. Vac. Sci. Technol. B*, **6**, 2286–2289.

Christl, I., Imseng, M., Tatti, E., Frommer, J., Viti, C., Giovannetti, L. & Kretzschmar, R. (2012). *Geomicrobiol. J.* **29**, 173–185.

Coffey, T., Urquhart, S. G. & Ade, H. (2002). *J. Electron Spectrosc. Relat. Phenom.* **122**, 65–78.

Darwin, C. R. (1862). *On the various contrivances by which British and foreign orchids are fertilised by insects, and on the good effects of intercrossing.* London: John Murray.

Engel, A. (1991). *Annu. Rev. Biophys. Biophys. Chem.* **20**, 79–108.

Fakra, S., Kilcoyne, A. L. D. & Tyliszczak, T. (2004). *AIP Conf. Proc.* **705**, 973–976.

Fink, R. H., Hub, C. & Tzvetkov, G. (2009). *Acta Phys. Pol. A*, **115**, 462–466.

Henderson, R. (1990). *Proc. R. Soc. London B*, **241**, 6–8.

Henderson, R. (1995). *Q. Rev. Biophys.* **28**, 171–193.

Henke, B. L., Gullikson, E. M. & Davis, J. C. (1993). *At. Data Nucl. Data Tables*, **54**, 181–342.

Hitchcock, A. P., Stöver, H. D. H., Croll, L. M. & Childs, R. F. (2005). *Aust. J. Chem.* **58**, 423–432.

Howells, M. R., Beetz, T., Chapman, H. N., Cui, C., Holton, J. M., Jacobsen, C. J., Kirz, J., Lima, E., Marchesini, S., Miao, H., Sayre, D., Shapiro, D. A., Spence, J. C. H. & Starodub, D. (2009). *J. Electron Spectrosc. Relat. Phenom.* **170**, 4–12.

Kilcoyne, A. L. D., Tyliszczak, T., Steele, W. F., Fakra, S., Hitchcock, P., Franck, K., Anderson, E., Harteneck, B., Rightor, E. G., Mitchell, G. E., Hitchcock, A. P., Yang, L., Warwick, T. & Ade, H. (2003). *J. Synchrotron Rad.* **10**, 125–136.

Kirz, J., Jacobsen, C. & Howells, M. (1995). *Q. Rev. Biophys.* **28**, 33–130.

Kourkoutis, L. F., Plitzko, J. M. & Baumeister, W. (2012). *Annu. Rev. Mater. Res.* **42**, 33–58.

Krause, M. O. (1979). *J. Phys. Chem. Ref. Data*, **8**, 307–327.

Larabell, C. A. & Nugent, K. A. (2010). *Curr. Opin. Struc. Biol.* **20**, 623–631.

Leontowich, A. F. G. & Hitchcock, A. P. (2011). *Appl. Phys. A*, **103**, 1–11.

Leontowich, A. F. G., Hitchcock, A. P., Tyliszczak, T., Weigand, M., Wang, J. & Karunakaran, C. (2012). *J. Synchrotron Rad.* **19**, 976–987.

Leung, B. O., Brash, J. L. & Hitchcock, A. P. (2010). *Materials*, **3**, 3911–3938.

Maser, J., Osanna, A., Wang, Y., Jacobsen, C., Kirz, J., Spector, S., Winn, B. & Tennant, D. (2000). *J. Microsc.* **197**, 68–79.

Meents, A., Gutmann, S., Wagner, A. & Schulze-Briese, C. (2010). *Proc. Natl Acad. Sci. USA*, **107**, 1094–1099.

Mroczkowski, S. & Lichtman, D. (1985). *J. Vac. Sci. Technol. A*, **3**, 1860–1865.

Nikjoo, H., O'Neill, P., Goodhead, D. T. & Terrissol, M. (1997). *Int. J. Radiat. Biol.* **71**, 467–483.

Rightor, E. G., Hitchcock, A. P., Ade, H., Leapman, R. D., Urquhart, S. G., Smith, A. P., Mitchell, G., Fischer, D., Shin, H. J. & Warwick, T. (1997). *J. Phys. Chem. B*, **101**, 1950–1960.

Rousseau, M. E., Hernández Cruz, D., West, M. M., Hitchcock, A. P. & Pézolet, M. (2007). *J. Am. Chem. Soc.* **129**, 3897–3905.

Sayre, D., Kirz, J., Feder, R., Kim, D. M. & Spiller, E. (1977). *Ultramicroscopy*, **2**, 337–349.

Schneider, G. (1998). *Ultramicroscopy*, **75**, 85–104.

Späth, A., Minami, H., Suzuki, T. & Fink, R. H. (2014). *RSC Adv.* **4**, 3272–3277.

Tanuma, S., Powell, C. J. & Penn, D. R. (2011). *Surf. Interface Anal.* **43**, 689–713.

Teng, T. & Moffat, K. (2000). *J. Synchrotron Rad.* **7**, 313–317.

Toner, B., Fakra, S., Villalobos, M., Warwick, T. & Sposito, G. (2005). *Appl. Environ. Microbiol.* **71**, 1300–1310.

Tzvetkov, G., Späth, A. & Fink, R. H. (2014). *Radiat. Phys. Chem.* **103**, 84–88.

Vila-Comamala, J., Jefimovs, K., Raabe, J., Pilvi, T., Fink, R. H., Senoner, M., Maassdorf, A., Ritala, M. & David, C. (2009). *Ultramicroscopy*, **109**, 1360–1364.

Wang, J., Botton, G. A., West, M. M. & Hitchcock, A. P. (2009*a*). *J. Phys. Chem. B*, **113**, 1869–1876.

Wang, J., Morin, C., Li, L., Hitchcock, A. P., Scholl, A. & Doran, A. (2009*b*). *J. Electron Spectrosc. Relat. Phenom.* **170**, 25–36.

Wang, J., Stover, H. D. H. & Hitchcock, A. P. (2007). *J. Phys. Chem. C*, **111**, 16330–16338.

Wang, Z., Zhang, L., Guo, Z., Liu, L., Ji, J., Zhang, J., Chen, X., Liu, B., Zhang, J., Ding, Q., Wang, X., Zhao, W., Zhu, Z. & Yu, Y. (2012). *PLoS One*, **7**, e50314.

Warwick, T., Ade, H., Kilcoyne, D., Kritscher, M., Tyliszczak, T., Fakra, S., Hitchcock, A., Hitchcock, P. & Padmore, H. (2002). *J. Synchrotron Rad.* **9**, 254–257.

Yeh, J. J. (1993). *Atomic Calculations of Photoionization Cross Sections and Asymmetry Parameters.* Langhorne: Gordon and Breach.

Zhang, X., Jacobsen, C., Lindaas, S. & Williams, S. (1995). *J. Vac. Sci. Technol. B*, **13**, 1477–1483.

Ziaja, B., van der Spoel, D., Szöke, A. & Hajdu, J. (2001). *Phys. Rev. B*, **64**, 214104.

Zubavichus, Y., Shaporenko, A., Grunze, M. & Zharnikov, M. (2005). *J. Phys. Chem. A*, **109**, 6998–7000.